Nano-Micro Letters

e-ISSN 2150-5551
CN 31-2103/TB

ARTICLE

https://doi.org/10.1007/s40820-025-02044-0

Cite as
Nano-Micro Lett.
(2026) 18:192

Received: 4 August 2025
Accepted: 6 December 2025

Photocatalytic H_2O_2 Production over Ultrathin Layered Double Hydroxide with 3.92% Solar-to-H_2O_2 Efficiency

Yamin Xi[1], Zechun Lu[3], Tong Bao[1], Yingying Zou[1], Chaoqi Zhang[1], Chunhong Xia[1], Guangfeng Wei[3] ✉, Chengzhong Yu[1,2,4] ✉, Chao Liu[1,2,5] ✉

HIGHLIGHTS

- The use of layered double hydroxides for photocatalytic for H_2O_2 production is innovatively demonstrated.
- Facet-dependent spatial charge separation enables maximized carrier utilization efficiency.
- The unique role of intercalated nitrate in promoting electron-hole separation and facilitating intermolecular electron transfer is unveiled.
- A record-high H_2O_2 production rate of 28.7 mmol g^{-1} h^{-1} with 3.92% solar-to-chemical efficiency is achieved.

ABSTRACT Artificial photosynthesis of hydrogen peroxide (H_2O_2) from earth-abundant water and oxygen is a sustainable approach, however current photocatalysts suffer from low production rate and solar-to-chemical conversion efficiency (< 1.5%). Herein, we report that nickel–chromium layered double hydroxide with intercalated nitrate (NiCrOOH-NO_3) and a thickness of ~ 4.4 nm is an efficient photocatalyst, enabling a H_2O_2 production yield of 28.7 mmol g^{-1} h^{-1} under visible light irradiation with 3.92% solar-to-chemical conversion efficiency. Experimental and computational studies have revealed an inherent facet-dependent reduction–oxidation reaction behavior and spatial separation of photogenerated electrons and holes. An unexpected role of intercalated nitrate is demonstrated, which promotes excited electron—hole spatial separation and facilitates the electron transfer to oxygen intermediate via delocalization. This work provides understandings in the impact of nanostructure and anion in the design of advanced photocatalysts, paving the way toward practical synthesis of H_2O_2 using fully solar-driven renewable energy.

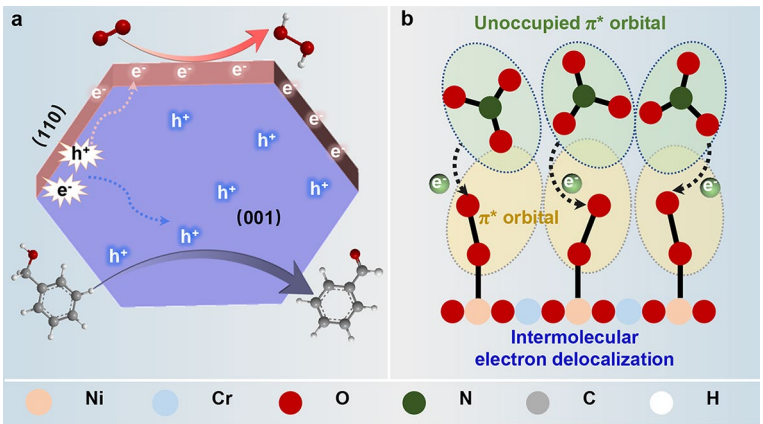

KEYWORDS Layered double hydroxide; Intercalated nitrate; Facet; Photocatalysis; Hydrogen peroxide

✉ Guangfeng Wei, weigf@tongji.edu.cn; Chengzhong Yu, c.yu@uq.edu.au; czyu@chem.ecnu.edu.cn; Chao Liu, cliu@chem.ecnu.edu.cn
[1] School of Chemistry and Molecular Engineering, East China Normal University, Shanghai 200241, People's Republic of China
[2] State Key Laboratory of Petroleum Molecular and Process Engineering, SKLPMPE, East China Normal University, Shanghai 200241, People's Republic of China
[3] Shanghai Key Laboratory of Chemical Assessment and Sustainability, School of Chemical, Science and Engineering, Tongji University, Shanghai 200092, People's Republic of China
[4] Australian Institute for Bioengineering and Nanotechnology, The University of Queensland, Brisbane, QLD 4072, Australia
[5] Shanghai Frontiers Science Center of Molecule Intelligent Syntheses, School of Chemistry and Molecular Engineering, East China Normal University, Shanghai 200241, People's Republic of China

Published online: 12 January 2026

Shanghai Jiao Tong University Press

Springer

1 Introduction

Hydrogen peroxide (H_2O_2) is an essential chemical with broad applications in chemical synthesis, environmental protection, medical disinfection, etc. [1, 2]. The industrial production of H_2O_2 is predominately achieved by the anthraquinone process, which suffers from high energy consumption and waste discharge [3]. As an alternative, the photocatalytic two-electron oxygen reduction reaction ($2e^-$ ORR) driven by solar energy emerges as a direct, contaminant-free and sustainable approach for on-site H_2O_2 production [4]. To date, numerous semiconducting materials such as metal sulfides [5], metal oxides [6], graphitic carbon nitride (g-C_3N_4) [7], metal–organic frameworks (MOFs) [8] and covalent organic frameworks (COFs) [9] have been reported for H_2O_2 production. However, the overall performance is unsatisfactory with low H_2O_2 production rate (< 20 mmol g^{-1} h^{-1}) and low solar-to-chemical conversion (SCC) efficiency (< 2.3% with only solar energy input), mainly due to insufficient utilization of photogenerated carriers and charge separation [10]. The development of effective $2e^-$ ORR photocatalysts for H_2O_2 production remains a challenge.

Ultrathin two-dimensional (2D) nanomaterials constitute an important class of advanced nanomaterials, featuring sheet-like structures with the lateral size over 100 nm but the thickness typically less than 5 nm [11, 12]. A plenty of ultrathin 2D nanomaterials such as graphitic carbon nitride [13], transition metal dichalcogenides [14], bismuth oxybromide [15], covalent-organic frameworks [16], and metal phosphorus trichalcogenides [17] have been fabricated with extraordinary properties and versatile applications. Layered double hydroxides (LDHs) are another type of 2D nanomaterials and photocatalysts [18]. Known as hydrotalcite-like anionic clay, LDHs are comprised of divalent and trivalent metal cations coordinated with hydroxide ions and intercalated with charge-compensating anions (e.g., NO_3^-, Cl^-) [19, 20]. To date, LDHs have been extensively studied as photocatalysts for water splitting [20], CO_2 reduction [21], N_2 fixation [22] and pollutant degradation [23], however their use in photocatalytic H_2O_2 production is rarely reported. Moreover, in the pursuit of high-performance LDH-based photocatalysts with various structural modification strategies (e.g., heterometal doping [24], defect engineering [25], cocatalyst loading [26] and heterojunction construction [27]), the impact of the intrinsic nanostructure (e.g., well-defined facet exposure) and interlayered anion on the photocatalytic properties of LDHs is largely overlooked.

Herein, we report nitrate anion (NO_3^-) intercalated NiCr-LDH ultrathin nanosheets (NiCrOOH-NO_3) as a highly efficient photocatalyst for $2e^-$ ORR to H_2O_2 coupled with benzyl alcohol oxidation reaction (BAOR) to benzaldehyde (BAD). Experimental results combined with theoretical calculations reveal the facet-dependent catalytic behavior with $2e^-$ ORR on (110) planes and BAOR on (001) planes, inducing the directional migration of photogenerated carriers and enhancing the charge separation (Scheme 1a). Besides, the intermolecular electron delocalization between unoccupied π* orbital of interlayered NO_3^- and π* orbital of adsorbed O_2 can promote the formation of electron–hole pairs and facilitate the transfer of photogenerated electron to oxygen intermediate (Scheme 1b). By virtue of the rational design at both nano and molecular scales, the NiCrOOH-NO_3 photocatalyst exhibits a record-high performance with a H_2O_2 production rate of 28.7 mmol g^{-1} h^{-1} and a SCC efficiency of 3.92% with only solar energy input. For the coupled BAOR, a high BAD yield of 27.6 mmol g^{-1} h^{-1} is achieved. Notably, both the $2e^-$ ORR and BAOR performances are superior than the reported photocatalysts.

2 Experimental Section

2.1 Materials

$Ni(NO_3)_2{\cdot}6H_2O$, $Cr(NO_3)_3{\cdot}9H_2O$, $NiCl_2{\cdot}6H_2O$, $CrCl_3{\cdot}6H_2O$ and $C_8H_5KO_4$ were obtained from Shanghai Titan Scientific Co., Ltd. Benzyl alcohol (BA, AR), KI and NaOH were purchased from Sigma-Aldrich. 30% hydrogen peroxide aqueous solution was supplied by Sinopharm Chemical Reagent Co., Ltd. All chemicals were used as received without further purification. Doubly distilled water was used in all experiments.

2.2 Preparation of NiCrOOH-NO_3, NiCrOOH-NO_3-T and NiCrOOH-Cl Nanosheets

2.2.1 Synthesis of NiCrOOH-NO_3 Nanosheets

5 mmol of $Ni(NO_3)_2{\cdot}6H_2O$ and 2.5 mmol of $Cr(NO_3)_3{\cdot}9H_2O$ were dissolved in 9 mL of deionized water (solution A). NaOH was dissolved in 9 mL of deionized water to give a 3 M

https://doi.org/10.1007/s40820-025-02044-0

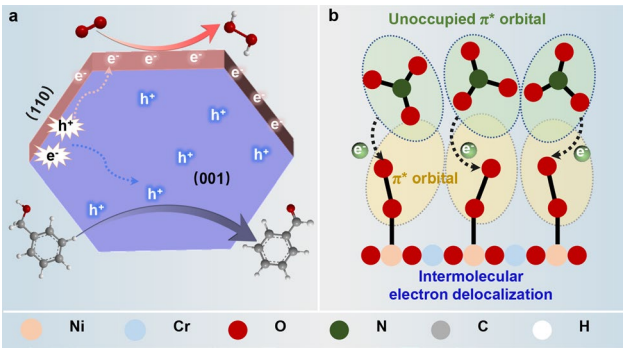

Scheme 1 Schematic illustration of **a** facet-dependent redox reaction behavior and **b** intermolecular electron delocalization between NO_3^- and adsorbed O_2 of NiCrOOH-NO_3

alkaline solution (solution B). Then, solution B was rapidly added into solution A and stirred rapidly at room temperature for 1 min. Then, the mixed solution was transferred into a Teflon-lined stainless-steek autoclave and kept at 120 °C for 12 h. After cooling down to room temperature, the solid products were collected by centrifugation, washed three times with deionized water and ethanol, and drying overnight. The final products were obtained and denoted as NiCrOOH-NO_3.

2.2.2 Synthesis of NiCrOOH-NO_3-T Nanosheets

NiCrOOH-NO_3-T was prepared by the similar procedure except that the reaction time was extended to 48 h. Through the same washing process of NiCrOOH-NO_3, the sample NiCrOOH-NO_3-T was obtained.

2.2.3 Synthesis of NiCrOOH-Cl Nanosheets

NiCrOOH-Cl was prepared by the similar procedure except that the $NiCl_2{\cdot}6H_2O$, $CrCl_3{\cdot}6H_2O$ were used as the starting materials. After reaction for 12 h at 120 °C, the NiCrOOH-Cl products were collected, washed with deionized water and ethanol for four times and dried overnight.

3 Results and Discussion

3.1 Structural Characterizations

Ultrathin NiCrOOH-NO_3 nanosheets were prepared using mixed metal nitrate precursors and NaOH as a co-precipitation agent. Atomic force microscopy (AFM) and transmission electron microscopy (TEM) techniques were used to characterize the morphology and structure of NiCrOOH-NO_3. AFM image shows that NiCrOOH-NO_3 possesses a uniform nanosheet morphology (Fig. 1a), the height profiles reveal an average thickness of ~ 4.4 nm (Fig. 1b). Under TEM observation, NiCrOOH-NO_3 displays a flake-like structure with an average diameter of ~ 100 nm (Fig. 1c) and a nearly hexagonal shape (Fig. 1d). The selected-area electron diffraction (SAED) pattern reveals hexagonally arrayed spots, indicating a highly ordered hexagonal structure along the [001] direction (Fig. 1e). By corelating the TEM image and SAED pattern, the side edges of the nanosheet are identified as the {110} planes of NiCrOOH-NO_3. In the high-resolution TEM (HRTEM) image (Fig. 1f), the clear lattice fringes with planar distance of 0.15 nm are also assigned to the (110) planes of NiCrOOH-NO_3 [21]. Further, under scanning transmission electron microscopy (STEM) mode, the high-angle annular dark-field (HAADF) and corresponding energy-dispersive X-ray spectroscopy (EDX) elemental mapping images demonstrate the homogeneous distribution of Ni, Cr, N, and O elements in the NiCrOOH-NO_3 nanosheets with a hexagonal shape (Fig. 1g–k).

The crystallinity of NiCrOOH-NO_3 is characterized using X-ray diffraction (XRD). As shown in the XRD pattern (Fig. 1l), the peaks of NiCrOOH-NO_3 observed at $2\theta = 10.18°$, 21.3°, 34.7°, and 60.6° can be indexed to the (003), (006), (012), and (110) diffractions of a hydrotalcite-like structure (PDF#52–1626) [28]. The interlayer spacing (d_{003}) of NiCrOOH-NO_3 is calculated to be 0.87 nm, indicating that one NiCrOOH-NO_3 nanosheet is consisted of five layers. The chemical composition and valence state of NiCrOOH-NO_3 were analyzed by X-ray photoelectron spectroscopy (XPS). In the XPS survey spectrum of NiCrOOH-NO_3 (Fig. S1, Table S1), Ni, Cr, O, and N elements were detected with a NO_3^-/metal molar ratio of ~ 0.33. In the Ni 2*p* spectrum of NiCrOOH-NO_3 (Fig. 1m), two peaks of $2p_{3/2}$ and $2p_{1/2}$ states of Ni^{2+} at 856.12 and 873.76 eV are deconvoluted, with two satellite peaks at 861.76 and 879.72 eV. The Cr 2*p* spectrum (Fig. 1n) exhibits two peaks assigned to $2p_{3/2}$ and $2p_{1/2}$ orbitals of Cr^{3+} at 577.00 and 586.87 eV, and two satellite peaks at 578.82 and 588.78 eV, respectively. For N 1*s* spectrum (Fig. 1o), the peak located at 406.55 eV is attributed to the intercalated NO_3^- ions. Figure 1p displays the O 2*p* spectrum, where two peaks corresponding to the lattice H_2O, metal-hydroxyl (M–OH) and M–O bond

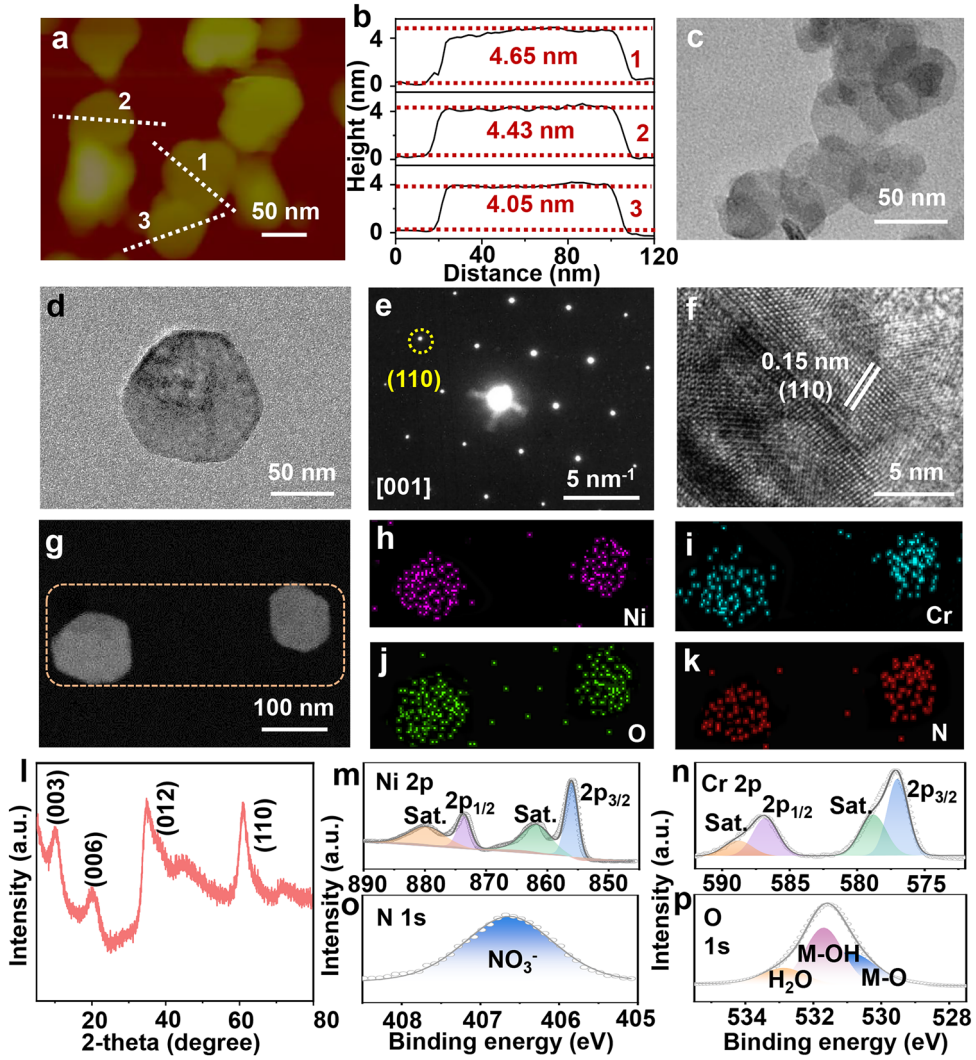

Fig. 1 **a** AFM image and **b** height profiles of NiCrOOH-NO_3 nanosheets. **c**, **d** TEM, **e**, **f** SAED and HRTEM, **g** HADDF-STEM and element mapping images, **l** XRD pattern of NiCrOOH-NO_3 nanosheets. High-resolution XPS spectra of **m** Ni 2*p*, **n** Cr 2*p*, **o** N 1*s* and **p** O 1*s* of NiCrOOH-NO_3

can be deconvoluted at 532.87, 531.69 and 530.95 eV. The attenuated total reflectance Fourier transform infrared (ATR-FTIR) spectrum of NiCrOOH-NO_3 is presented in Fig. S2. The broad band located at 3496 cm^{-1} belongs to the O–H stretching vibration from interlayer water molecules in LDH [29]. Besides, the sharp bands at 1634 and 1335 cm^{-1} are attributed to the vibration modes of hydroxyl groups and interlayer NO_3^- anions, respectively.

Thermogravimetric analysis (TGA) was performed to further study the chemical compositions. In the TGA curve of NiCrOOH-NO_3 (Fig. S3), the first-stage weight loss of ≈ 12.97% at 100–180 °C is associated with the removal of interlayer lattice H_2O. The shrinkage of hydroxide layers results in the second-stage weight loss of ≈ 14.10% between 180 and 280 °C. The further weight loss of 12.00% after 280 °C is ascribed to the decomposition of NO_3^- anions [28, 30]. According to TGA analyses, the formulas of NiCrOOH-NO_3 can be calculated as $Ni_{2.00}Cr_{0.99}(OH)_{5.98}[NO_3^-]_{0.99}{\cdot}2.75H_2O$. In addition, the atomic proportion of Ni and Cr is measured to be 2.02 in NiCrOOH-NO_3 by inductively coupled plasma atomic emission spectrometry (ICP-AES), respectively. In combination with the contents of H, N and O elements determined by elemental analysis (EA, Table S2), the chemical composition of NiCrOOH-NO_3 was speculated as $Ni_{2.00}Cr_{0.99}N_{0.99}O_{11.47}H_{11.48}$, in good agreement with the TGA findings.

https://doi.org/10.1007/s40820-025-02044-0

For comparison, a thicker nanosheet was synthesized by increasing the reaction time (denoted NiCrOOH-NO_3-T). As shown in Fig. S4a, b, the average thickness of the NiCrOOH-NO_3-T is *ca.* 37.9 nm. From the TEM image (Fig. S4c), the hexagonal morphology with a lateral size of ~ 150 nm is clearly seen for NiCrOOH-NO_3-T. Except for the thickness, the crystalline structure and electronic states of NiCrOOH-NO_3-T are almost identical with NiCrOOH-NO_3, as evidenced by the XRD pattern and XPS spectra in Fig. S5. In addition, the Brunauer–Emmett–Teller (BET) specific surface area of NiCrOOH-NO_3-T was calculated to be 60.2 $m^2\ g^{-1}$ by N_2 sorption measurements, slightly lower than that of NiCrOOH-NO_3 (93.1 $m^2\ g^{-1}$, Table S3).

To explore the optical absorption properties and band structures of the samples, ultraviolet–visible diffuse reflectance spectroscopy (UV–Vis DRS) measurement was conducted. As shown in Fig. S7a, the light absorption intensity of NiCrOOH-NO_3 is stronger than NiCrOOH-NO_3-T. The absorption band in the region 200–300 nm is attributed to the ligand-to metal charge transfer, *i.e.,* O2$p \rightarrow$ Ni-3d-t_{2g}/Cr-3d-t_{2g}. Two more bands located at 420 and 580 nm are assigned to the spin-forbidden transitions ($^3A_{2g}(F) \rightarrow {}^1E_g(D)$ and $^3A_{2g}(F) \rightarrow {}^1T_{2g}(D)$, respectivey) [22, 24]. The bandgaps (E_g) of NiCrOOH-NO_3 and NiCrOOH-NO_3-T were calculated to be 2.37 and 2.48 eV, respectively, using the Kubelka–Munk equation (Fig. S7b). Further according to the Mott–Schottky plots (Fig. S7c), the conduction band (CB) values of NiCrOOH-NO_3 and NiCrOOH-NO_3-T are determined as -0.42 and -0.39 V vs. NHE, respectively [31]. Therefore, the valence band (VB) values can be calculated (NiCrOOH-NO_3: 1.95 eV; NiCrOOH-NO_3-T: 2.09 eV) and the band structures are illustrated in Fig. S7d. Both samples show sufficient thermodynamic driving force for photocatalytic 2e^- ORR and BAOR [32, 33].

3.2 Catalytic Performance Evaluation

The photocatalytic performance of coupled reaction of 2e^- ORR to H_2O_2 and BAOR to benzaldehyde (BAD) was evaluated in an oxygen-saturated BA solution under UV–visible light irradiation (320 nm < λ < 780 nm, 0.20 W cm^{-2}, Fig. S8). The yields of BAD and H_2O_2 were quantified by high-performance liquid chromatography (HPLC) and iodometry method, respectively, and the corresponding standard curves are shown in Fig. S9. The H_2O_2 and BAD yields as a function of time are depicted in Figs. 2a and S10. NiCrOOH-NO_3 produces 286.6 μmol of H_2O_2 and 275.9 μmol of BAD in 1 h (Fig. 2a), respectively, significantly higher than those of NiCrOOH-NO_3-T (76.9 μmol of H_2O_2 yield, 51.5 μmol of BAD, Fig. S10), indicating the enhanced activity of NiCrOOH-NO_3. Furthermore, the H_2O_2 yield quantified by colorimetry method is consistent with the result obtained from iodometry method (Figs. S11 and S12). The high H_2O_2 production rate of 28.7 mmol $g^{-1}\ h^{-1}$ (Fig. 2b) is superior to previously reported photocatalysts in both pure water and water-benzyl alcohol systems, and even reaches the level of electrocatalytic 2e^- ORR systems (Fig. 2d). For BAD, the yield of 27.6 mmol $g^{-1}\ h^{-1}$ for NiCrOOH-NO_3 also exceeds the reported values (Fig. S13). Furthermore, an isotope labeling experiment was conducted by using $^{18}O_2/H_2{}^{16}O$ and $^{16}O_2/H_2{}^{18}O$ as raw materials. Gas chromatography-mass spectrometry (GC–MS) was employed to detect O_2 generated by the decomposition of H_2O_2. In the spectrum recorded by feeding $^{18}O_2$ and $H_2{}^{16}O$ (Fig. S14), a distinct peak assigned to $^{18}O_2$ is observed at m/z = 36. When changing the reactants into $^{16}O_2$ and $H_2{}^{18}O$, only a trace amount of $^{18}O_2$ is detected, indicating that the oxygen in H_2O_2 is derived from O_2.

The light utilization efficiency of NiCrOOH-NO_3 was also assessed by measuring the apparent quantum yield (AQY). Under the irradiation of monochromatic light from 365 to 650 nm (Fig. 2c), the AQY value of NiCrOOH-NO_3 follows the same trend with the absorption spectrum. The peak value of AQY reaches 33.7% at 400 nm for NiCrOOH-NO_3. After correction for scattering and absorption using the integrating sphere method, the absorbed-photon-to-chemical efficiency (APCE) for H_2O_2 production was determined to be 68.78% at 400 nm (Table S4) [34]. Moreover, under the illumination of simulated sunlight (AM 1.5G), the solar conversion chemical efficiency (SCC) of NiCrOOH-NO_3 was measured to be 3.92% under optimized stirring speed (800 rpm) and optical depth (120 mL of reaction solution) (Figs. S16 and S17). Notably, the SCC efficiency was calculated based on the photocatalytic 2e^- ORR pathway specifically for H_2O_2 production. Both the AQY and SCC are higher than previously reported photocatalysts (Fig. 2d; Tables S5 and S6) [1, 10, 35–61]. In addition, negligible amounts of H_2O_2 were detected in the reaction systems without catalysts or light irradiation, verifying that H_2O_2 is predominantly produced from photocatalytic 2e^- ORR (Fig. S18). When conducting photocatalysis in Ar-saturated H_2O, almost no H_2O_2 was produced by NiCrOOH-NO_3 (Fig. S18), excluding the possibility of direct two-electron water oxidation reaction

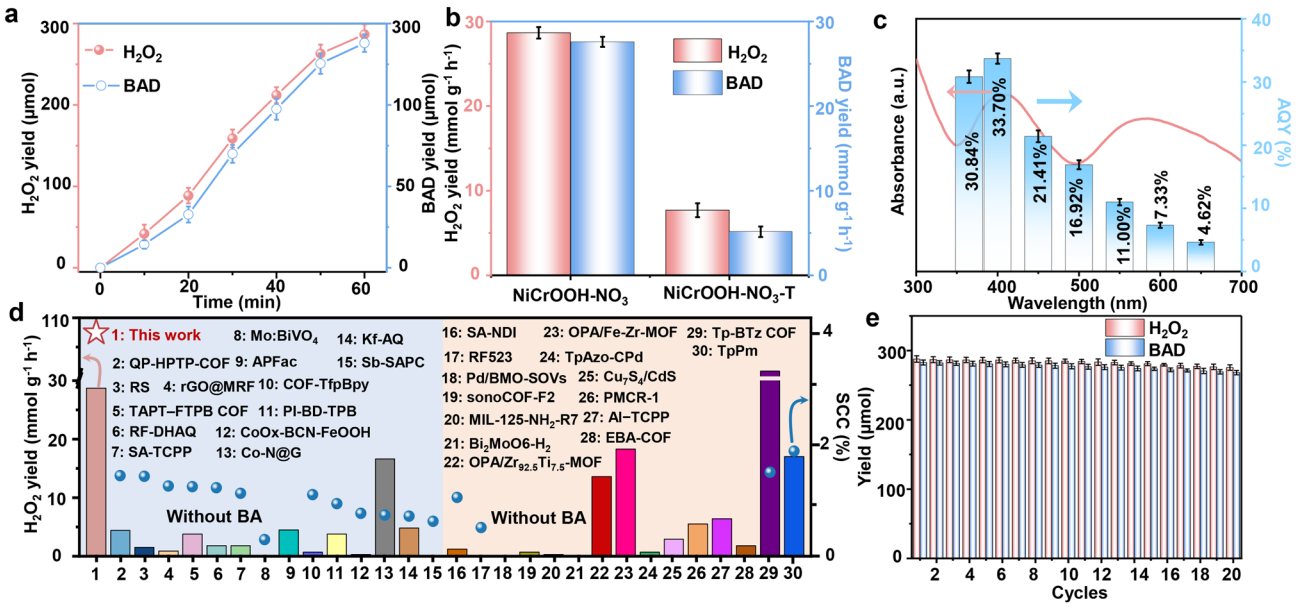

Fig. 2 **a** Time course of H_2O_2 and BAD contents during the photocatalytic reaction over NiCrOOH-NO_3. **b** H_2O_2 and BAD yield rates of NiCrOOH-NO_3 and NiCrOOH-NO_3-T. **c** Wavelength-dependent AQY of NiCrOOH-NO_3. **d** Comparison of the H_2O_2 yield, AQY, and SCC of NiCrOOH-NO_3 and other recently reported photocatalysts. **e** H_2O_2 and BAD yield of NiCrOOH-NO_3 during recycling stability test

($2e^-$ WOR). Except for high activity, NiCrOOH-NO_3 also possesses high photocatalytic durability with negligible decline of both ORR and BAOR yields after twenty consecutive reaction cycles with each cycle lasting for 1 h (Fig. 2e). XRD, FTIR and XPS (Figs. S19-S22; Tables S1 and S7) characterizations of NiCrOOH-NO_3 collected after reaction reveal well-retained morphology, composition and element contents. In the supernatant after reaction, only trace amount of Ni and Cr were detected (Table S7). Furthermore, the nitrate retention in used NiCrOOH-NO_3 was calculated to be 98.99% according to the XPS results (Table S1), further demonstrating the structural robustness of NiCrOOH-NO_3.

3.3 Mechanistic Studies

To track the reaction process of photocatalytic $2e^-$ ORR coupled with BAOR over NiCrOOH-NO_3, in situ irradiated XPS (ISIXPS) and in situ diffuse reflectance infrared Fourier transform spectroscopy (DRIFTS) measurements were employed. The in situ XPS spectra of Ni 2*p*, Cr 2*p*, O 1*s*, and N 1*s* are shown in Fig. S23. Compared to the Ni 2*p* spectrum in the dark without O_2, the Ni $2p_{3/2}$ peak of NiCrOOH-NO_3 exhibits a positive shift of 0.33 eV after introducing O_2 for 20 min, which may be attributed to the chemisorption of O_2 on Ni sites. After 5 min of light irradiation, the binding energy of Ni $2p_{3/2}$ peak increases by 0.75 eV due to the electron depletion for photocatalytic $2e^-$ ORR. Different from Ni, the binding energies of Cr peaks are almost identical in the spectra recorded with and without O_2, indicating that Cr is not the active site for O_2 adsorption. For O 1*s*, the spectra before and after introducing O_2 are also similar in darkness. Upon irradiation, an additional peak of M-OOH emerges at 532.30 eV, verifying the formation of the *OOH intermediate on the catalyst surface. Moreover, compared to the N 1*s* spectrum in darkness, the peak of intercalated NO_3^- in the spectrum under irradiation shows a negative shift of 0.21 eV, indicating an increased electron density of NO_3^- with the accumulation of photogenerated electrons. The DRIFT spectrum in the dark (Fig. 3a) shows the peaks assigned to the bands of O–O bonding of O_2 (1465 cm^{-1}), H_2O (1650 cm^{-1}) [62], and the stretching vibrations of C=C (1490 and 1555 cm^{-1}) and C–O (1027 cm^{-1}) bonds in BA [36]. By applying light irradiation for 20 min, the peak intensity of the above four reactants is reduced with three new peaks of C=O stretching mode of BAD (1700 cm^{-1}), *OOH (1378 cm^{-1}) and *HOOH (1233 cm^{-1}) generated [41, 45]. By prolonging the irradiation time to 40 and 60 min, the

https://doi.org/10.1007/s40820-025-02044-0

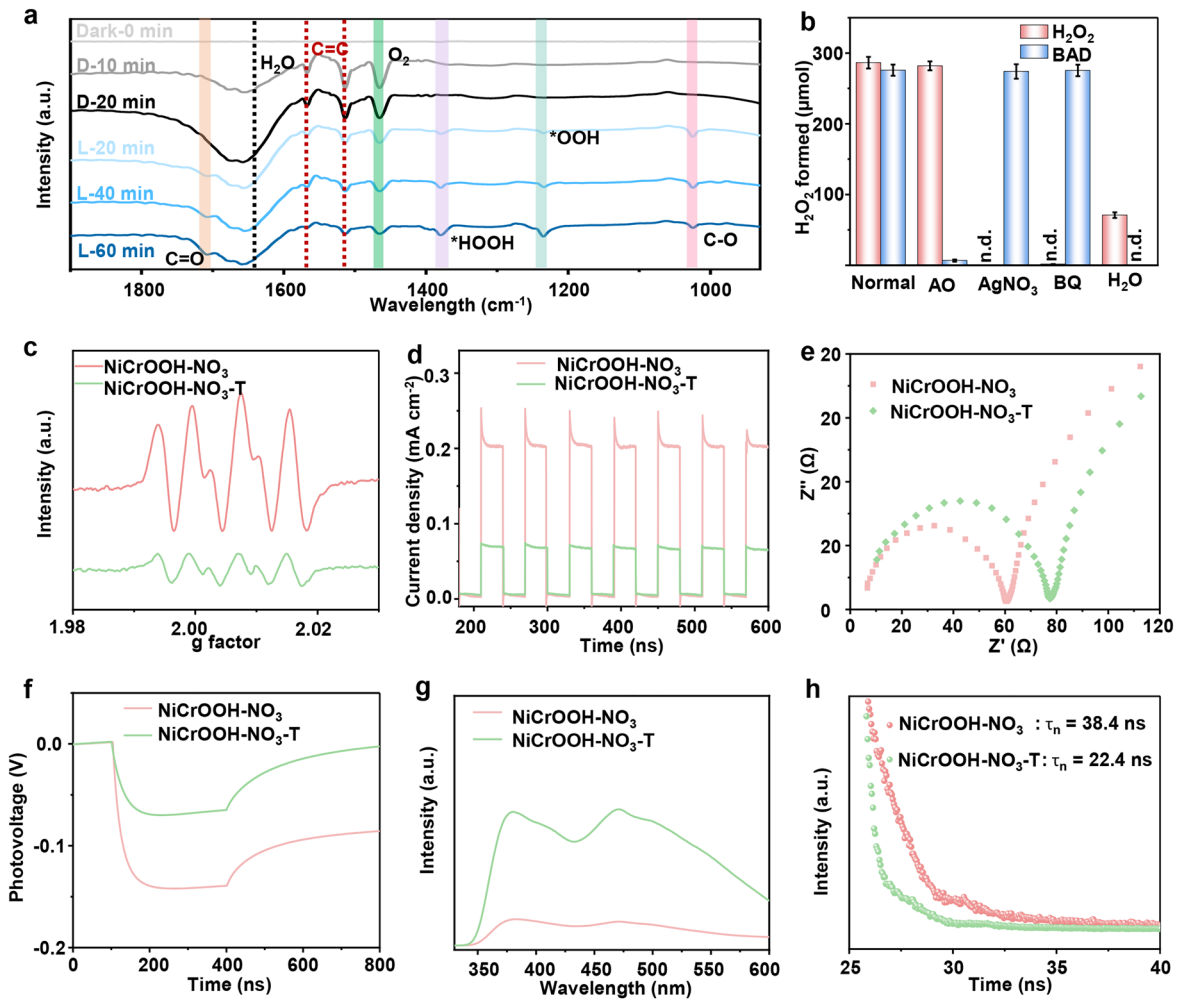

Fig. 3 **a** In situ DRFTS spectra of NiCrOOH-NO_3. **b** Effect of different reactive species scavengers on the photocatalytic H_2O_2 and BAD yield of NiCrOOH-NO_3. **c** ESR signals of DMPO-$\cdot O_2^-$ of NiCrOOH-NO_3 and NiCrOOH-NO_3-T. **d** Transient photocurrent responses, **e** EIS curves, **f** OCVD curves, **g** PL spectra and **h** TRPL spectra of NiCrOOH-NO_3 and NiCrOOH-NO_3-T

peak intensity of the intermediates and products is continuously elevated with further consumed raw materials, suggesting the occurrence of $2e^-$ ORR to H_2O_2 and BAOR to BAD.

Subsequently, a series of control experiments were conducted under varying reaction conditions. As displayed in Fig. 3b, the yield of BAD dramatically decreases when adding ammonium oxalate (AO, a hole scavenger) into the reaction system. By introducing $AgNO_3$ (an electron scavenger), the H_2O_2 evolution is nearly terminated. These observations indicate that the production of H_2O_2 and BAD is mainly driven by the photoexcited electrons and holes, respectively [45]. The presence of p-benzoquinone (BQ), a scavenger of $\cdot O_2^-$, also greatly impedes the H_2O_2 production, implying that the $\cdot O_2^-$ radical is the vital intermediate for H_2O_2 formation [63], in accordance with the observations of in-situ DRIFTS spectra. The electron paramagnetic resonance (EPR) spectra collected by using 5,5-Dimethyl-1-pyrroline N oxide (DMPO) as a spin trap (Fig. 3c) show the characteristic signals of $\cdot O_2^-$ radicals under illumination, further supporting a two-step single-electron reduction mechanism with $\cdot O_2^-$ as reaction intermediate ($O_2 + e^- \rightarrow \cdot O_2^-$, $\cdot O_2^- + 2H^+ + e^- \rightarrow H_2O_2$) for H_2O_2 production [38]. Additionally, the NiCrOOH-NO_3 exhibits stronger signal intensities than NiCrOOH-NO_3-T (Fig. 3c), corresponding to the enhanced activity of NiCrOOH-NO_3. Moreover, the H_2O_2 yield is dramatically reduced in the absence of BA (Fig. 3b), suggesting the crucial role of BA in facilitating O_2 to H_2O_2 conversion.

To understand the reasons of enhanced properties of $NiCrOOH\text{-}NO_3$, the activity and selectivity of ORR over $NiCrOOH\text{-}NO_3$ and $NiCrOOH\text{-}NO_3$-T were investigated via rotating ring-disk electrode (RRDE) measurements [64]. As shown in Fig. S24, the linear sweep voltammetry (LSV) curves include the ORR current at the disk electrode (solid line) and the H_2O_2 oxidation current at the ring electrode (dashed line). Compared to $NiCrOOH\text{-}NO_3$-T, $NiCrOOH\text{-}NO_3$ delivers higher current densities of both ORR and H_2O_2 oxidation, showing a higher activity. Combining the disk and ring currents, the $2e^-$ ORR selectivity of $NiCrOOH\text{-}NO_3$ and $NiCrOOH\text{-}NO_3$-T was calculated to be 93.3 and 95.9% (Fig. S24b), respectively, favoring the $2e^-$ ORR pathway.

Afterward, photoelectrochemical and photoluminescence (PL) measurements were employed for determining the charge transfer efficiencies and dynamics. The photocurrent response profiles in Fig. 3d manifest higher photocurrent density of $NiCrOOH\text{-}NO_3$ than $NiCrOOH\text{-}NO_3$-T, indicating more efficient separation of photoinduced electron–hole pairs of $NiCrOOH\text{-}NO_3$. The Nyquist plots (Fig. 3e) obtained by electrochemical impedance spectroscopy (EIS) test show that the arc radius of $NiCrOOH\text{-}NO_3$ is smaller than that of $NiCrOOH\text{-}NO_3$-T, revealing a lower charge transfer resistance and faster charge transfer rate. To further evaluate the kinetic characteristics of photogenerated charges, the open-circuit voltage decay (OCVD) curves of $NiCrOOH\text{-}NO_3$ and $NiCrOOH\text{-}NO_3$-T (Fig. 3f) were recorded [65]. Under light illumination, $NiCrOOH\text{-}NO_3$ exhibits a higher open-circuit voltage than $NiCrOOH\text{-}NO_3$-T. When the light is switched off, the slower photovoltage decay of $NiCrOOH\text{-}NO_3$ suggests a longer lifetime of photoexcited carriers. Figure 3g displays the steady PL spectra. Compared to $NiCrOOH\text{-}NO_3$-T, the PL intensity of $NiCrOOH\text{-}NO_3$ is significantly reduced, indicating the suppressed recombination of photogenerated charge carriers. As a commonly used technique for investigating the electron–hole pair separation kinetics, time-resolved photoluminescence spectroscopy (TRPL) test was also performed. As shown in Fig. 3h, the fluorescence lifetime of $NiCrOOH\text{-}NO_3$ is estimated to be 38.4 ns by double exponential fitting method, longer than that of $NiCrOOH\text{-}NO_3$-T (22.4 ns), further verifying the improved charge separation ability of $NiCrOOH\text{-}NO_3$.

To provide understandings of the photocatalyst structure-performance relationship, comprehensive density functional theory (DFT) calculations were conducted. Firstly, we aimed to understand the impact of facet exposure on the photocatalytic performance. The reaction profiles and optimized intermediates structures of the ORR and BAOR on the (110) and (001) surfaces of $NiCrOOH\text{-}NO_3$ are shown in Figs. 4 and S25. For $2e^-$ ORR, step I involves the leaving of a surface coordination $*H_2O$ and *OH on (110) and (001) surfaces, respectively, to create an unsaturated Ni^* site (Fig. 4a). Subsequently, O_2 is adsorbed on the exposed metal sites to form O_{2ad} (step II) [66]. Then, the reduction in O_{2ad} to OOH_{ad} by photo-generated electrons (step III) and further reduction in OOH_{ad} generate H_2O_2 (step IV) to complete a $2e^-$ ORR cycle. Alternatively, OOH_{ad} can be reduced to O_{ad} and OH_{ad}, forming H_2O in a competitive $4e^-$ ORR pathway [67]. From the free energy change (ΔG) in each step of the ORR process (Fig. 4c), step I is the rate-determining step (RDS). Moreover, the ΔG of Step I over the (110) facet of $NiCrOOH\text{-}NO_3$ is − 0.01 eV, lower than that for the (001) facet (1.83 eV) with exposure of hydroxyl groups, indicating that the (110) facet is a preferred site for the ORR process. In addition, the ΔG of $OOH_{ad} \rightarrow O_{ad}$ over (110) facet is 0.2 eV higher than the ΔG of $OOH_{ad} \rightarrow H_2O_2$. In contrast, the ΔG of $OOH_{ad} \rightarrow O_{ad}$ is negative while the ΔG of $OOH_{ad} \rightarrow H_2O_2$ is positive over the (001) facet. The calculation results indicate that the $2e^-$ ORR pathway is more favorable on the (110) facet than the (001) facet.

For a BAOR cycle, BA is adsorbed on the catalyst in step I (Fig. 4b). The formed $Ph\text{-}CH_2OH_{ad}$ is preferentially oxidized to $Ph\text{-}CHOH_{ad}$ by the holes (h^+) in step II. Then, $Ph\text{-}CHOH_{ad}$ is further oxidized to $Ph\text{-}CHO_{ad}$ in step III before the release of the final Ph-CHO product in step IV. It is noted that the ΔG of the first three steps is consistently lower over the (001) surface of $NiCrOOH\text{-}NO_3$ than the (110) surface (Fig. 4d), mainly due to the hydrogen bonding interactions between the hydroxyl groups on the (001) facet of the catalyst and the oxygen-containing groups in $Ph\text{-}CH_2OH_{ad}$, $Ph\text{-}CHOH_{ad}$ and $Ph\text{-}CHO_{ad}$ intermediates (Fig. 4d), suggesting that the (001) facets are kinetically favorable for BA oxidation.

The above results indicate that the photo-generated electrons are mainly located on the (110) facet for reduction reactions while the holes on the (001) facet for oxidation reactions. To further support the facet-dependent charge separation, Kelvin probe force microscopy (KPFM) analysis was performed under dark and illumination conditions. Figure S26 shows the topographic image of $NiCrOOH\text{-}NO_3$ nanosheets. A statistical histogram is presented by

 https://doi.org/10.1007/s40820-025-02044-0

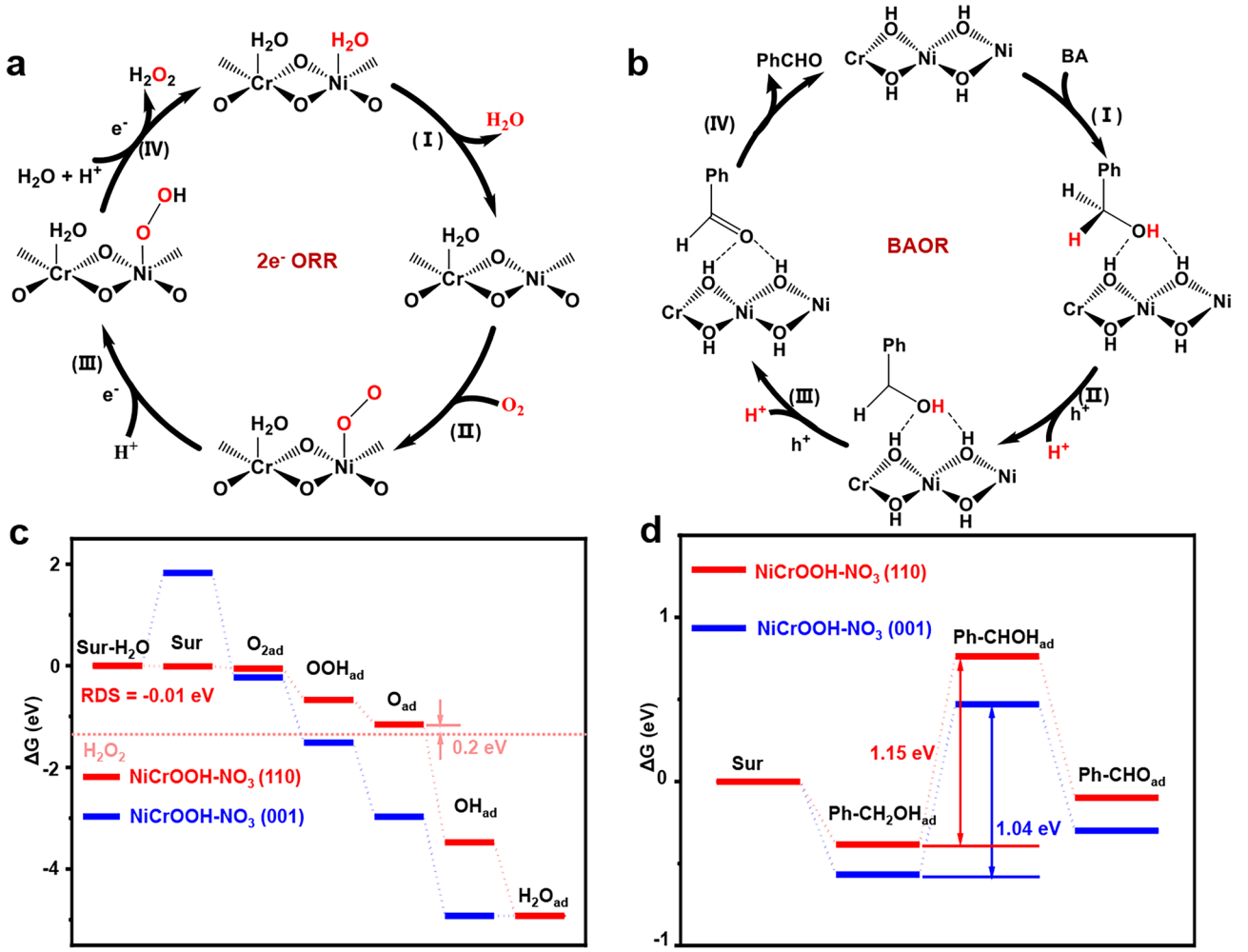

Fig. 4 The proposed 2e⁻ ORR **a** and BAOR **b** catalytic cycle diagrams over NiCrOOH-NO_3. The reaction profiles of **c** the ORR and **d** BAOR on NiCrOOH-NO_3

measuring the light-induced potential difference of eight independent nanosheets (Fig. S26a-c). Elevated surface potential of (001) facet in NiCrOOH-NO_3 is observed under illumination (average 31.20 mV) compared to that in dark (average 11.95 mV), suggesting the accumulation of photogenerated holes on the (001) facet. Moreover, from the production rates of H_2O_2 and BAD, the ratio of consumed electrons and holes is estimated to be 1/0.96 for NiCrOOH-NO_3, closer to 1/1 than that for NiCrOOH-NO_3-T (1/0.67). This observation is consistent with the simulation results, suggesting that the higher exposure of {001} planes in NiCrOOH-NO_3 than NiCrOOH-NO_3-T facilitates the hole consumption and BAOR. Thus, the spatially separated (110) and (001) facets with optimized facet exposure ratio enables the efficient utilization of photogenerated electrons and holes with enhanced photocatalytic performance.

Secondly, to elucidate the structural basis of the improved 2e⁻ ORR and BAOR performance of NiCrOOH-NO_3, the profiles of total density of states (TDOS) and projected density of states (PDOS) are illustrated in Fig. 5a, and the highest occupied molecular orbital (HOMO)-lowest unoccupied molecular orbital (LUMO) analysis in Fig. 5b. For NiCrOOH-NO_3, the valance band maximum (VBM) is mainly dictated by the Ni–O–Cr orbital (indicated in red), while the conduction band maximum (CBM) is predominantly contributed by the N–O orbitals of NO_3^- (blue). Thus, the holes are in the Ni–O–Cr units (HOMO) while the excited electrons are localized in

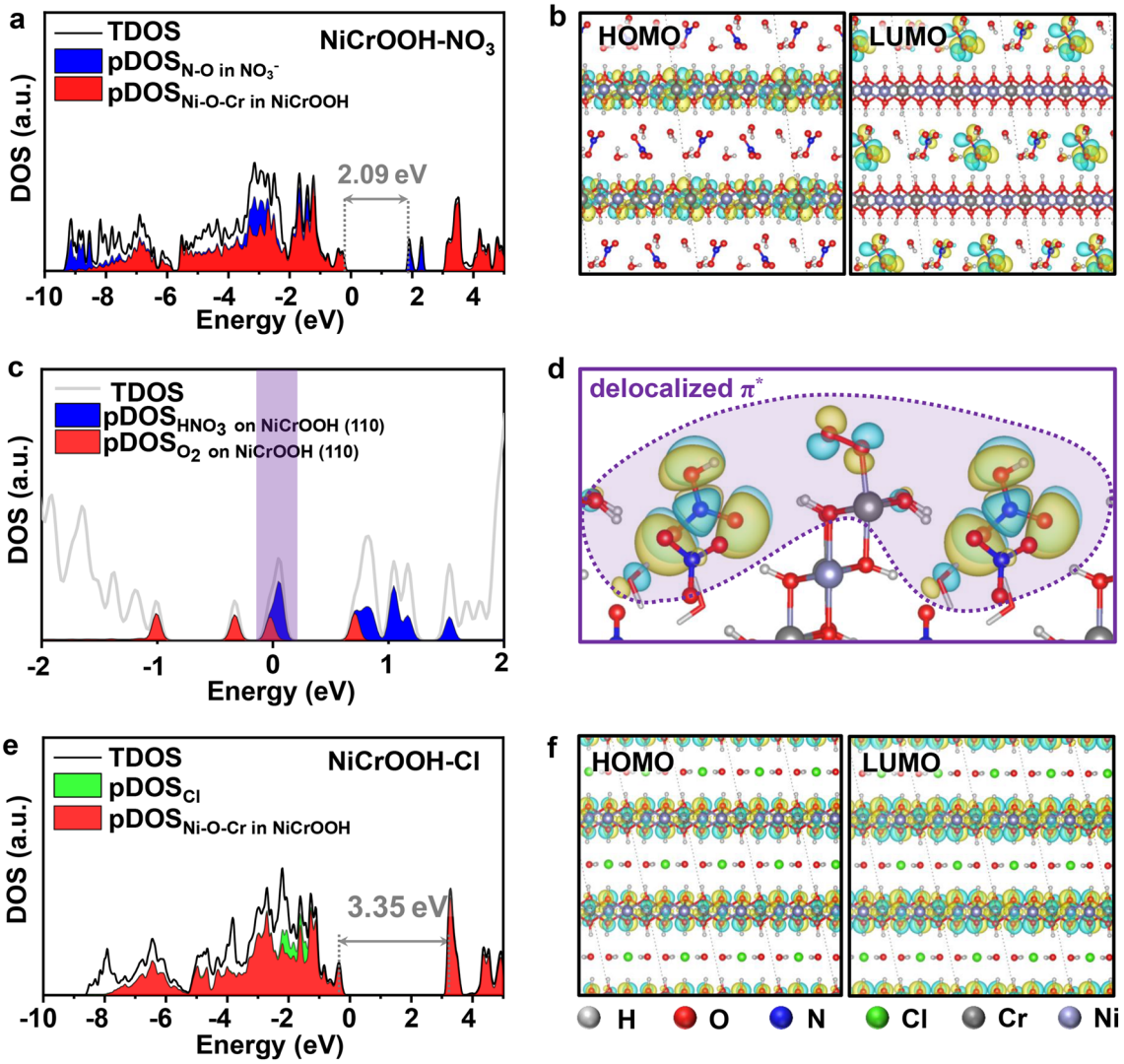

Fig. 5 **a** TDOS and pDOS of NO_3^- and Ni–O–Cr layer for NiCrOOH-NO_3. **b** HOMO and LUMO isosurfaces of NiCrOOH-NO_3. **c** TDOS and pDOS of NO_3^- and adsorbed O_2 on (110) surface of NiCrOOH-NO_3 in the presence of additional $H^+ + e^-$ pair. **d** Wavefunction isosurfaces of the states at the VBM of NiCrOOH-NO_3 in the presence of adsorbed O_2 and additional $H^+ + e^-$ pair. **e** TDOS and pDOS of Cl^- and Ni–O–Cr layer for NiCrOOH-Cl. **f** HOMO and LUMO isosurfaces of NiCrOOH-Cl. In the wavefunction isosurfaces, the yellow and green isosurfaces represent the positive and negative regions of the wave function, respectively

antibonding π^* orbitals of interlayer NO_3^- (LUMO). The bandgap of NiCrOOH-NO_3 is calculated to be 2.09 eV, close to the experimental findings (Fig. S7b).

Next, the DOS analysis in the presence of both adsorbed O_2 molecule and additional $H^+ + e^-$ pair was studied in the photocatalytic process (Fig. 5c). Compared to the original NiCrOOH-NO_3, the introduction of adsorbed O_2 molecule and additional $H^+ + e^-$ results in a significant change of the DOS profile. The VBM (shown in purple) is shifted to the previously unoccupied π^* orbital of NO_3^- (blue) that overlaps with the bonding peak of π^* orbital of adsorbed O_2 molecule (red). The wavefunction isosurfaces of the VBM state (Fig. 5d) illustrate that the adsorbed oxygen molecules can acquire electrons through the coupled π^* orbitals, thereby facilitating subsequent reduction reactions. These results suggest the crucial role of interlayer NO_3^- in electron–hole generation upon photoexcitation and intramolecular electron transfer in manipulating the photocatalytic performance.

For comparison, a control sample NiCrOOH-Cl with interlayer Cl^- was prepared and characterized (see details in Figs. S27 and S28) [68]. As shown in Figs. S27 and

 https://doi.org/10.1007/s40820-025-02044-0

S28; Table S3, NiCrOOH-Cl possesses similar morphology, crystal structure and specific surface area with NiCrOH-NO_3. The photochemical results show that H_2O_2 (11.1 mmol g^{-1} h^{-1}) and BAD (10.5 mmol g^{-1} h^{-1}) yields of NiCrOOH-Cl are both inferior than NiCrOOH-NO_3 (Fig. S29). Besides, the 2e$^-$ ORR selectivity of NiCrOOH-Cl was determined as 93.0% (Fig. S30), close to that of NiCrOOH-NO_3 (93.3%). The lower photocurrent response and fluorescence lifetime, larger impedance radius and higher fluorescence intensity (Fig. S31) further indicate that the electron hole separation capacity of NiCrOOH-Cl is lower than that of NiCrOOH-NO_3. Different from NiCrOOH-NO_3, both the VBM and CBM of NiCrOOH-Cl are contributed by the Ni–O–Cr orbitals (Fig. 5e). From the pDOS profile (Fig. 5f), both the photoexcited holes and electrons are located in the Ni–O–Cr units, leading to insufficient charge separation. The O_2 adsorption on NiCrOOH-Cl follows a side-on mode, the same as that on NiCrOOH-NO_3 (Fig. S32). These results further indicate the unique role of interlayer NO_3^- in not only facilitating the ORR process but also promoting electron–hole separation.

4 Conclusions

In summary, ultrathin NiCrOOH-NO_3 nanosheets have been designed as an efficient photocatalyst for 2e$^-$ ORR integrated with BAOR. Systematical investigations reveal the synergistic roles of facet engineering and NO_3^- intercalation in improving photocatalytic performance. The spatial separation of active sites for 2e$^-$ ORR on (110) planes and BAOR on (001) planes facilitate the directional migration of photogenerated electrons and holes, promoting charge separation. The interlayered NO_3^- ions favor the electron–hole pair generation and promote the electron transfer to oxygen intermediate via intermolecular electron delocalization. As a result, the NiCrOOH-NO_3 photocatalyst exhibits record-high performance with a H_2O_2 production rate of 28.7 mmol g^{-1} h^{-1} and a SCC efficiency of 3.92%. Our findings have paved the way for the development of advanced LDH structures and high-performance 2e$^-$ ORR photocatalysts.

Acknowledgements The authors acknowledge support from the National Natural Science Foundation of China (NSFC 21905092, 22475072 and 22075085) and the Fundamental Research Funds for the Central Universities. This work was supported by the Shanghai Frontiers Science Center of Molecule Intelligent Syntheses. East China Normal University Multifunctional Platform for Innovation (004).

Author Contributions Y.X., G.W., C.Y. and C.L. conceived the idea. Y.Z. and C.L. performed most of material synthesis and characterizations and photochemical measurements. T.B., Z.Y., C.Z. and X.X. took part in the photocatalytic measurements and discussions. Z.L, G.W. carried out the DFT calculations. G.W., C.Y. and C.L. supervised the work and directed the research. All authors were involved in the discussions and reviewed the manuscript.

Declarations

Conflict of interest The authors declare no interest conflict. They have no known competing financial interests or personal relationships that could have appeared to influence the work reported in this paper.

Supplementary Information The online version contains supplementary material available at https://doi.org/10.1007/s40820-025-02044-0.

References

1. J. Cheng, Y. Wu, W. Zhang, L. Wang, X. Wu et al., Unlocking topological effects in covalent organic frameworks for high-performance photosynthesis of hydrogen peroxide. Adv. Mater. **37**(1), 2410247 (2025). https://doi.org/10.1002/adma.202410247
2. J. Yang, X. Zeng, M. Tebyetekerwa, Z. Wang, C. Bie et al., Engineering 2D photocatalysts for solar hydrogen peroxide production. Adv. Energy Mater. **14**(23), 2400740 (2024). https://doi.org/10.1002/aenm.202400740
3. J.M. Campos-Martin, G. Blanco-Brieva, J.L.G. Fierro, Hydrogen peroxide synthesis: an outlook beyond the anthraquinone process. Angew. Chem. Int. Ed. **45**(42), 6962–6984 (2006). https://doi.org/10.1002/anie.200503779
4. T. Freese, J.T. Meijer, B.L. Feringa, S.B. Beil, An organic perspective on photocatalytic production of hydrogen peroxide.

Nat. Catal. **6**(7), 553–558 (2023). https://doi.org/10.1038/s41929-023-00980-x

5. C. Liu, T. Bao, L. Yuan, C. Zhang, J. Wang et al., Semiconducting MOF@ZnS heterostructures for photocatalytic hydrogen peroxide production: heterojunction coverage matters. Adv. Funct. Mater. **32**(15), 2111404 (2022). https://doi.org/10.1002/adfm.202111404
6. C. Xia, L. Yuan, H. Song, C. Zhang, Z. Li et al., Spatial specific Janus S-scheme photocatalyst with enhanced H_2O_2 production performance. Small **19**(29), e2300292 (2023). https://doi.org/10.1002/smll.202300292
7. F. He, Y. Lu, Y. Wu, S. Wang, Y. Zhang et al., Rejoint of carbon nitride fragments into multi-interfacial order-disorder homojunction for robust photo-driven generation of H_2O_2. Adv. Mater. **36**(9), e2307490 (2024). https://doi.org/10.1002/adma.202307490
8. J.Y. Choi, B. Check, X. Fang, S. Blum, H.T.B. Pham et al., Photocatalytic hydrogen peroxide production through functionalized semiconductive metal-organic frameworks. J. Am. Chem. Soc. **146**(16), 11319–11327 (2024). https://doi.org/10.1021/jacs.4c00681
9. A. Chakraborty, A. Alam, U. Pal, A. Sinha, S. Das et al., Enhancing photocatalytic hydrogen peroxide generation by tuning hydrazone linkage density in covalent organic frameworks. Nat. Commun. **16**(1), 503 (2025). https://doi.org/10.1038/s41467-025-55894-y
10. C. Zhao, H. Li, Y. Yin, W. Tian, X. Yan et al., Non-radical mediated photocatalytic H_2O_2 synthesis in conjugate-enhanced phenolic resins with ultrafast charge separation. Angew. Chem. Int. Ed. **64**(9), e202420895 (2025). https://doi.org/10.1002/anie.202420895
11. C. Tan, X. Cao, X.-J. Wu, Q. He, J. Yang et al., Recent advances in ultrathin two-dimensional nanomaterials. Chem. Rev. **117**(9), 6225–6331 (2017). https://doi.org/10.1021/acs.chemrev.6b00558
12. H. Zhang, Ultrathin two-dimensional nanomaterials. ACS Nano **9**(10), 9451–9469 (2015). https://doi.org/10.1021/acsnano.5b05040
13. Q. Li, Y. Jiao, Y. Tang, J. Zhou, B. Wu et al., Shear stress triggers ultrathin-nanosheet carbon nitride assembly for photocatalytic H_2O_2 production coupled with selective alcohol oxidation. J. Am. Chem. Soc. **145**(38), 20837–20848 (2023). https://doi.org/10.1021/jacs.3c05234
14. L. Kuo, V.K. Sangwan, S.V. Rangnekar, T.-C. Chu, D. Lam et al., All-printed ultrahigh-responsivity MoS_2 nanosheet photodetectors enabled by megasonic exfoliation. Adv. Mater. **34**(34), e2203772 (2022). https://doi.org/10.1002/adma.202203772
15. M. Guan, C. Xiao, J. Zhang, S. Fan, R. An et al., Vacancy associates promoting solar-driven photocatalytic activity of ultrathin bismuth oxychloride nanosheets. J. Am. Chem. Soc. **135**(28), 10411–10417 (2013). https://doi.org/10.1021/ja402956f
16. W. Liu, X. Li, C. Wang, H. Pan, W. Liu et al., A scalable general synthetic approach toward ultrathin imine-linked two-dimensional covalent organic framework nanosheets for photocatalytic CO_2 reduction. J. Am. Chem. Soc. **141**(43), 17431–17440 (2019). https://doi.org/10.1021/jacs.9b09502
17. J. Ran, H. Zhang, S. Fu, M. Jaroniec, J. Shan et al., $NiPS_3$ ultrathin nanosheets as versatile platform advancing highly active photocatalytic H_2 production. Nat. Commun. **13**(1), 4600 (2022). https://doi.org/10.1038/s41467-022-32256-6
18. C. Ning, S. Bai, J. Wang, Z. Li, Z. Han et al., Review of photo- and electro-catalytic multi-metallic layered double hydroxides. Coord. Chem. Rev. **480**, 215008 (2023). https://doi.org/10.1016/j.ccr.2022.215008
19. Y. Wang, M. Zhang, Y. Liu, Z. Zheng, B. Liu et al., Recent advances on transition-metal-based layered double hydroxides nanosheets for electrocatalytic energy conversion. Adv. Sci. **10**(13), 2207519 (2023). https://doi.org/10.1002/advs.202207519
20. Y. Zhao, X. Jia, G.I.N. Waterhouse, L.-Z. Wu, C.-H. Tung et al., Layered double hydroxide nanostructured photocatalysts for renewable energy production. Adv. Energy Mater. **6**(6), 1501974 (2016). https://doi.org/10.1002/aenm.201501974
21. S. Li, Z. Li, J. Yue, H. Wang, Y. Wang et al., Photocatalytic CO_2 reduction by near-infrared-light (1200 nm) irradiation and a ruthenium-intercalated NiAl-layered double hydroxide. Angew. Chem. Int. Ed. **63**(45), e202407638 (2024). https://doi.org/10.1002/anie.202407638
22. Y. Zhao, L. Zheng, R. Shi, S. Zhang, X. Bian et al., Alkali etching of layered double hydroxide nanosheets for enhanced photocatalytic N_2 reduction to NH_3. Adv. Energy Mater. **10**(34), 2002199 (2020). https://doi.org/10.1002/aenm.202002199
23. M. Yu, D. Liu, L. Wang, J. Xia, J. Ren et al., A Zn-Al-Zr layered double hydroxide/graphene oxide nanocomposite enables rapid photocatalytic removal of kanamycin-resistance bacteria and genes *via* nano-confinement effects. Appl. Catal. B Environ. Energy **350**, 123922 (2024). https://doi.org/10.1016/j.apcatb.2024.123922
24. S. Zhang, Y. Zhao, R. Shi, C. Zhou, G.I.N. Waterhouse et al., Efficient photocatalytic nitrogen fixation over Cuδ+-modified defective ZnAl-layered double hydroxide nanosheets. Adv. Energy Mater. **10**(8), 1901973 (2020). https://doi.org/10.1002/aenm.201901973
25. Y. Zhao, G. Chen, T. Bian, C. Zhou, G.I.N. Waterhouse et al., Defect-rich ultrathin ZnAl-layered double hydroxide nanosheets for efficient photoreduction of CO_2 to CO with water. Adv. Mater. **27**(47), 7824–7831 (2015). https://doi.org/10.1002/adma.201503730
26. A. Cai, G. Hu, W. Chen, S. An, B. Qi et al., Single-atom Pt anchored polyoxometalate as electron-proton shuttle for efficient photoreduction of CO_2 to CH_4 catalyzed by NiCo layered doubled hydroxide. Small **21**(2), 2410343 (2025). https://doi.org/10.1002/smll.202410343
27. X. Han, B. Lu, X. Huang, C. Liu, S. Chen et al., Novel p- and n-type S-scheme heterojunction photocatalyst for boosted CO_2 photoreduction activity. Appl. Catal. B Environ. **316**, 121587 (2022). https://doi.org/10.1016/j.apcatb.2022.121587
28. X. Feng, X. Li, H. Luo, B. Su, J. Ma, Facile synthesis of Ni-based layered double hydroxides with superior photocatalytic performance for tetracycline antibiotic degradation. J. Solid

 https://doi.org/10.1007/s40820-025-02044-0

State Chem. **307**, 122827 (2022). https://doi.org/10.1016/j.jssc.2021.122827

29. R. Wang, Z. Qiu, S. Wan, Y. Wang, Q. Liu et al., Insight into mechanism of divalent metal cations with different d-bands classification in layered double hydroxides for light-driven CO_2 reduction. Chem. Eng. J. **427**, 130863 (2022). https://doi.org/10.1016/j.cej.2021.130863
30. W. Kou, Z. Fang, H. Ding, W. Luo, C. Liu et al., Valence engineering boosts kinetics and storage capacity of layered double hydroxides for aqueous magnesium-ion batteries. Adv. Funct. Mater. **34**(41), 2406423 (2024). https://doi.org/10.1002/adfm.202406423
31. Y. Xi, Y. Xiang, T. Bao, Z. Li, C. Zhang et al., Nanoarchitectonics of S-scheme heterojunction photocatalysts: a nanohouse design improves photocatalytic nitrate reduction to ammonia performance. Angew. Chem. Int. Ed. **63**(38), e202409163 (2024). https://doi.org/10.1002/anie.202409163
32. B.C. Moon, B. Bayarkhuu, K.A.I. Zhang, D.K. Lee, J. Byun, Solar-driven H_2O_2 production *via* cooperative auto- and photocatalytic oxidation in fine-tuned reaction media. Energy Environ. Sci. **15**(12), 5082–5092 (2022). https://doi.org/10.1039/D2EE02504C
33. J. Qiu, K. Meng, Y. Zhang, B. Cheng, J. Zhang et al., COF/In_2S_3 S-scheme photocatalyst with enhanced light absorption and H_2O_2-production activity and fs-TA investigation. Adv. Mater. **36**(24), 2400288 (2024). https://doi.org/10.1002/adma.202400288
34. Y. Zhang, Y. Li, X. Xin, Y. Wang, P. Guo et al., Internal quantum efficiency higher than 100% achieved by combining doping and quantum effects for photocatalytic overall water splitting. Nat. Energy **8**(5), 504–514 (2023). https://doi.org/10.1038/s41560-023-01242-7
35. W. Chi, Y. Dong, B. Liu, C. Pan, J. Zhang et al., A photocatalytic redox cycle over a polyimide catalyst drives efficient solar-to-H_2O_2 conversion. Nat. Commun. **15**(1), 5316 (2024). https://doi.org/10.1038/s41467-024-49663-6
36. R. Ji, Y. Dong, X. Sun, P. Li, R. Zhang et al., Novel A–D–a type naphthalenediimide supramolecule for H_2O_2 photosynthesis with solar-to-chemical conversion 1.03%. Adv. Energy Mater. **14**(30), 2401437 (2024). https://doi.org/10.1002/aenm.202401437
37. M. Kou, Y. Wang, Y. Xu, L. Ye, Y. Huang et al., Molecularly engineered covalent organic frameworks for hydrogen peroxide photosynthesis. Angew. Chem. Int. Ed. **61**(19), e202200413 (2022). https://doi.org/10.1002/anie.202200413
38. P. Liu, T. Liang, Y. Li, Z. Zhang, Z. Li et al., Photocatalytic H_2O_2 production over boron-doped g-C_3N_4 containing coordinatively unsaturated FeOOH sites and CoO_x clusters. Nat. Commun. **15**(1), 9224 (2024). https://doi.org/10.1038/s41467-024-53482-0
39. T. Liu, Z. Pan, J.J.M. Vequizo, K. Kato, B. Wu et al., Overall photosynthesis of H_2O_2 by an inorganic semiconductor. Nat. Commun. **13**, 1034 (2022). https://doi.org/10.1038/s41467-022-28686-x
40. Y. Liu, L. Li, Z. Sang, H. Tan, N. Ye et al., Enhanced hydrogen peroxide photosynthesis in covalent organic frameworks through induced asymmetric electron distribution. Nat. Synth. **4**(1), 134–141 (2025). https://doi.org/10.1038/s44160-024-00644-z
41. Y. Shiraishi, T. Takii, T. Hagi, S. Mori, Y. Kofuji et al., Resorcinol–formaldehyde resins as metal-free semiconductor photocatalysts for solar-to-hydrogen peroxide energy conversion. Nat. Mater. **18**(9), 985–993 (2019). https://doi.org/10.1038/s41563-019-0398-0
42. Z. Teng, Q. Zhang, H. Yang, K. Kato, W. Yang et al., Atomically dispersed antimony on carbon nitride for the artificial photosynthesis of hydrogen peroxide. Nat. Catal. **4**(5), 374–384 (2021). https://doi.org/10.1038/s41929-021-00605-1
43. Q. Tian, X.-K. Zeng, C. Zhao, L.-Y. Jing, X.-W. Zhang et al., Exceptional photocatalytic hydrogen peroxide production from sandwich-structured graphene interlayered phenolic resins nanosheets with mesoporous channels. Adv. Funct. Mater. **33**(21), 2213173 (2023). https://doi.org/10.1002/adfm.202213173
44. W. Wang, Q. Song, Q. Luo, L. Li, X. Huo et al., Photothermal-enabled single-atom catalysts for high-efficiency hydrogen peroxide photosynthesis from natural seawater. Nat. Commun. **14**(1), 2493 (2023). https://doi.org/10.1038/s41467-023-38211-3
45. X. Wang, X. Yang, C. Zhao, Y. Pi, X. Li et al., Ambient preparation of benzoxazine-based phenolic resins enables long-term sustainable photosynthesis of hydrogen peroxide. Angew. Chem. Int. Ed. **62**(23), e202302829 (2023). https://doi.org/10.1002/anie.202302829
46. X. Zhang, S. Cheng, C. Chen, X. Wen, J. Miao et al., Ketoanthraquinone covalent organic framework for H_2O_2 photosynthesis with oxygen and alkaline water. Nat. Commun. **15**(1), 2649 (2024). https://doi.org/10.1038/s41467-024-47023-y
47. Y. Zhang, C. Pan, G. Bian, J. Xu, Y. Dong et al., H_2O_2 generation from O_2 and H_2O on a near-infrared absorbing porphyrin supramolecular photocatalyst. Nat. Energy **8**(4), 361–371 (2023). https://doi.org/10.1038/s41560-023-01218-7
48. C. Zhao, X. Wang, Y. Yin, W. Tian, G. Zeng et al., Molecular level modulation of anthraquinone-containing resorcinol-formaldehyde resin photocatalysts for H_2O_2 production with exceeding 1.2% efficiency. Angew. Chem. Int. Ed. **62**(12), e202218318 (2023). https://doi.org/10.1002/anie.202218318
49. C. Chen, G. Qiu, T. Wang, Z. Zheng, M. Huang et al., Modulating oxygen vacancies on bismuth-molybdate hierarchical hollow microspheres for photocatalytic selective alcohol oxidation with hydrogen peroxide production. J. Colloid Interface Sci. **592**, 1–12 (2021). https://doi.org/10.1016/j.jcis.2021.02.036
50. X. Chen, Y. Kuwahara, K. Mori, C. Louis, H. Yamashita, A hydrophobic titanium doped zirconium-based metal organic framework for photocatalytic hydrogen peroxide production in a two-phase system. J. Mater. Chem. A **8**(4), 1904–1910 (2020). https://doi.org/10.1039/C9TA11120D
51. X. Chen, Y. Kuwahara, K. Mori, C. Louis, H. Yamashita, Heterometallic and hydrophobic metal–organic frameworks as durable photocatalysts for boosting hydrogen peroxide

production in a two-phase system. ACS Appl. Energy Mater. **4**(5), 4823–4830 (2021). https://doi.org/10.1021/acsaem.1c00371

52. P. Das, J. Roeser, A. Thomas, Solar light driven H_2O_2 production and selective oxidations using a covalent organic framework photocatalyst prepared by a multicomponent reaction. Angew. Chem. Int. Ed. **62**(29), e202304349 (2023). https://doi.org/10.1002/anie.202304349
53. Y. Isaka, Y. Kawase, Y. Kuwahara, K. Mori, H. Yamashita, Two-phase system utilizing hydrophobic metal–organic frameworks (MOFs) for photocatalytic synthesis of hydrogen peroxide. Angew. Chem. Int. Ed. **58**(16), 5402–5406 (2019). https://doi.org/10.1002/anie.201901961
54. L. Li, X. Huo, S. Chen, Q. Luo, W. Wang et al., Solar-driven production of hydrogen peroxide and benzaldehyde in two-phase system by an interface-engineered Co_9S_8-$CoZnIn_2S_4$ heterostructure. Small **19**(38), 2301865 (2023). https://doi.org/10.1002/smll.202301865
55. A. Rodríguez-Camargo, M.W. Terban, M. Paetsch, E.A. Rico, D. Graf et al., Cyclopalladation of a covalent organic framework for near-infrared-light-driven photocatalytic hydrogen peroxide production. Nat. Synth. **4**(6), 710–719 (2025). https://doi.org/10.1038/s44160-024-00731-1
56. Z. Sun, X. Yang, X.-F. Yu, L. Xia, Y. Peng et al., Surface oxygen vacancies of Pd/Bi_2MoO_{6-x} acts as "Electron Bridge" to promote photocatalytic selective oxidation of alcohol. Appl. Catal. B Environ. **285**, 119790 (2021). https://doi.org/10.1016/j.apcatb.2020.119790
57. Z. Zheng, F. Han, B. Xing, X. Han, B. Li, Synthesis of Fe_3O_4@CdS@CQDs ternary core–shell heterostructures as a magnetically recoverable photocatalyst for selective alcohol oxidation coupled with H_2O_2 production. J. Colloid Interface Sci. **624**, 460–470 (2022). https://doi.org/10.1016/j.jcis.2022.05.161
58. X. Zeng, T. Wang, Z. Wang, M. Tebyetekerwa, Y. Liu et al., Fast photocatalytic hydrogen peroxide generation by singlet oxygen-engaged sequential excitation energy and electron-transfer process. ACS Catal. **14**(13), 9955–9968 (2024). https://doi.org/10.1021/acscatal.4c01591
59. L. Zhai, Z. Xie, C.-X. Cui, X. Yang, Q. Xu et al., Constructing synergistic triazine and acetylene cores in fully conjugated covalent organic frameworks for cascade photocatalytic H_2O_2 production. Chem. Mater. **34**(11), 5232–5240 (2022). https://doi.org/10.1021/acs.chemmater.2c00910
60. Z. Xue, B. Zhang, Q. Guo, Y. Wang, Q. Li et al., Sacrificial-agent-triggered mass transfer gating in covalent organic framework for hydrogen peroxide photocatalysis. Adv. Mater. **37**(42), e10201 (2025). https://doi.org/10.1002/adma.202510201
61. Z. Chen, H. Weng, C. Chu, D. Yao, Q. Li et al., Nitrogen heterocyclic covalent organic frameworks for efficient H_2O_2 photosynthesis and *in situ* water treatment. Nat. Commun. **16**(1), 6943 (2025). https://doi.org/10.1038/s41467-025-62371-z
62. S. Nayak, I.J. McPherson, K.A. Vincent, Adsorbed intermediates in oxygen reduction on platinum nanoparticles observed by in situ IR spectroscopy. Angew. Chem. Int. Ed. **130**(39), 13037–13040 (2018). https://doi.org/10.1002/ange.201804978
63. L. Yuan, P. Du, C. Zhang, Y. Xi, Y. Zou et al., Facet-dependent spatial separation of dual cocatalysts on MOF photocatalysts for H_2O_2 production coupling biomass oxidation with enhanced performance. Appl. Catal. B Environ. Energy **364**, 124855 (2025). https://doi.org/10.1016/j.apcatb.2024.124855
64. L. Yuan, Y. Zou, L. Zhao, C. Zhang, J. Wang et al., Unveiling the lattice distortion and electron-donating effects in methoxy-functionalized MOF photocatalysts for H_2O_2 production. Appl. Catal. B Environ. **318**, 121859 (2022). https://doi.org/10.1016/j.apcatb.2022.121859
65. Y. Deng, W. Liu, R. Xu, R. Gao, N. Huang et al., Reduction of superoxide radical intermediate by polydopamine for efficient hydrogen peroxide photosynthesis. Angew. Chem. Int. Ed. **63**(14), e202319216 (2024). https://doi.org/10.1002/anie.202319216
66. Y. Xi, Y. Xiang, C. Zhang, T. Bao, Y. Zou et al., Perfect is perfect: nickel Prussian blue analogue as a high-efficiency electrocatalyst for hydrogen peroxide production. Angew. Chem. Int. Ed. **64**(1), e202413866 (2025). https://doi.org/10.1002/anie.202413866
67. C. Zhang, L. Yuan, C. Liu, Z. Li, Y. Zou et al., Crystal engineering enables cobalt-based metal-organic frameworks as high-performance electrocatalysts for H_2O_2 production. J. Am. Chem. Soc. **145**(14), 7791–7799 (2023). https://doi.org/10.1021/jacs.2c11446
68. K. Wang, Y. Liu, Z. Ding, Z. Chen, X. Xu et al., Chloride pre-intercalated CoFe-layered double hydroxide as chloride ion capturing electrode for capacitive deionization. Chem. Eng. J. **433**, 133578 (2022). https://doi.org/10.1016/j.cej.2021.133578

 https://doi.org/10.1007/s40820-025-02044-0